Nanoscale



PAPER

View Article Online



Cite this: Nanoscale, 2024, 16, 16218

Improved electrochemical reduction of CO₂ to syngas with a highly exfoliated Ti₃C₂T_x MXene-gold composite†

Murugan Krishnan, a Aathilingam Vijayaprabhakaran and Murugavel Kathiresan to *a



Transforming carbon dioxide (CO₂) into valuable chemicals via electroreduction presents a sustainable and viable approach to mitigating excess CO2 in the atmosphere. This report provides fresh insights into the design of a new titanium-based MXene composite as a catalyst for the efficient conversion of CO₂ in a safe aqueous medium. Despite its excellent electrocatalytic activity towards CO2 reduction and high selectivity for CO production, the high cost of Au and the decline in catalytic activity on a larger scale hinder its large-scale CO2 conversion applications. In this research, we have successfully prepared an Au/ Ti₃C₂T_x composite and tested its catalytic activity in the electrochemical CO₂ reduction reaction (ECRR). The as-prepared composite features strong interactions between gold atoms and the MXene support, achieved through the formation of metal-oxygen/carbon bonds. The Au/ $Ti_3C_2T_x$ electrode demonstrated a significant current density of 17.3 mA cm⁻² at a potential of -0.42 V vs. RHE, in a CO₂ saturated atmosphere (faradaic efficiency: CO = 48.3% and $H_2 = 25.6\%$). Nyquist plots further indicated a reduction in the charge-transfer resistance of the Au/Ti₃C₂T_x layer, signifying rapid charge transfer between the Au and $Ti_3C_2T_x$. Furthermore, it is known that liquid crossover through the Gas Diffusion Electrode (GDE) significantly improves CO2 diffusion to catalyst active sites, thereby enhancing CO2 conversion efficiency. The goal of this work is to design an interface between metal and MXene so that CO₂ can be electroreduced to fuels and other useful chemical compounds with great selectivity.

Received 15th March 2024, Accepted 30th July 2024 DOI: 10.1039/d4nr01122h

rsc li/nanoscale

Introduction

The amount of carbon dioxide (CO₂) in the Earth's atmosphere has been rising over the past few decades; in 2016, it surpassed and remained above 400 parts per million (ppm) for the first time in human history.^{1,2} There is a correlation between the rise in global mean temperature anomalies, the consequent impacts of climate change and the increase in atmospheric CO₂ levels.³ It is therefore still a major task for the twenty-first century to develop cost-effective technologies that can reduce, trap, or use excessive anthropogenic CO₂ emissions. ⁴⁻⁶ One of the carbon capture and utilization technologies that has attracted interest recently is the electrochemical CO2 reduction reaction (ECRR), which uses both water and electricity to convert CO2 into useful compounds.7,8 CO2 may be reduced in the cathodic compartment to a number of products, including

† Electronic supplementary information (ESI) available. See DOI: https://doi.org/

carbons, depending on the type of modified catalyst. 9,10 However, the electrochemical CO2 transformation system has a relatively low energy efficiency for conversion resulting from its high overpotential to form transition states and poor selectivity among multiple competing processes. Therefore, it is crucial to develop catalytic electrodes¹¹ that can facilitate the transfer of electrons to the thermodynamically inert CO2 molecule in order to create reduced products selectively. Research indicates that gold (Au) is a particularly efficient electrocatalyst¹² that has a high Faraday efficiency (FE) and can convert CO2 to carbon monoxide (CO) at low overpotentials. 13-15 Nevertheless, the high cost and enormous potential for poisoning of Au restrict its widespread use. 16,17 Research using novel nanostructures 18,19 has shown that even small changes in the size, shape, or surface characteristics of metal nanoparticles (NPs)²⁰⁻²² have a significant impact on the ECRR activity. Size dependence on selectivity has been particularly proposed to be caused by the simultaneous competition of active centres for the ECRR. The intrinsic characteristics and the interaction that exists between the loaded catalyst and the support can have a major impact on the binary system's final catalytic activity. Porous or nanostructured architectures²³ provide a

syngas, formate (HCOO⁻), methane (CH₄), and other hydro-

10.1039/d4nr01122h

^aElectro Organic & Materials Electrochemistry Division, CSIR-Central Electrochemical Research Institute, Karaikudi - 630003, Tamil Nadu, India, E-mail: kathiresan@cecri.res.in ^bAcademy of Scientific and Innovative Research (AcSIR), Ghaziabad – 201002, India

Nanoscale Paper



Fig. 1 Schematic illustration of the preparation of Au/ $Ti_3C_2T_x$.

large surface area for the ECRR and improve support/substrate conductivity, which prevents resistance losses. These are examples of well-known strategies for improving electrocatalytic performances. 24,25 In contrast to other supports, Ti₃C₂T_x-MXene can improve ECRR performance because of its active and abundant adsorption sites, high electron density, high carrier mobility, tunable Fermi level, and 2D multilayered structure. $^{26-29}$ Moreover, $Ti_3C_2T_x$ can speed up the kinetics of the process and electron transfer by acting as a promoter.³⁰ Because Ti₃C₂T_x can be easily synthesized in large quantities from a variety of inexpensive, readily available precursors, and its degradation produces simply TiO2 and CO2, it is more viable for use in large-scale applications. 31-33 Ti₃C₂T_x enhanced with terminal functionalities ($T_x = O_2$, OH, and F) can provide readily available catalytic sites for reactant adsorption and reduce the binding energies of ECRR intermediates and products. Despite the fact that Ti₃C₂T_x has been used for ECRR applications for a long time, we anticipate that coupling Au NPs with it can dramatically enhance the ECRR performance. In order to overcome the main challenges of liquid reduction processes and enable upscaling, researchers have turned to gas-diffusion electrode³⁴ (when a porous, conductive support exists to hold the catalyst) based systems. A higher CO₂ concentration and a shorter diffusion path can result in commercially-relevant current densities. Unexpectedly, the Au/ $Ti_3C_2T_x$ catalyst functions as a gas-diffusion electrode (GDE) and presents a promising avenue for enhancing the overall performance of the ECRR under mild operating conditions.35,36 However, the doping of Au NPs into Ti₃C₂T_x for the ECRR has not been investigated yet.

In this study, we report the selective and stable electrore-duction of CO_2 to syngas using Au decorated MXene. To achieve high conversion efficiency, a gas-diffusion layer was prepared with $\mathrm{Au/Ti}_3\mathrm{C}_2\mathrm{T}_x$ and used as a cathode. The $\mathrm{Ti}_3\mathrm{C}_2\mathrm{T}_x$ catalyst was prepared by a simple etching method using HF/HCl and the etched MXene was composited with Au (Fig. 1). We report a binary system that uses $\mathrm{Ti}_3\mathrm{C}_2\mathrm{T}_x$ as the substrate and a secondary catalyst, with well-dispersed Au NPs acting as an ECRR catalyst. This thin-layered, exfoliated $\mathrm{Ti}_3\mathrm{C}_2\mathrm{T}_x$ is

perfect for adding well-dispersed Au NPs since Au/Au NPs exhibit remarkable efficacy in a variety of catalytic processes. The binary catalytic system, *i.e.*, Au NPs incorporated into ${\rm Ti_3C_2T_x}$, was demonstrated to be an excellent catalyst for the co-conversion of ${\rm CO_2}$ and ${\rm H_2O}$ to CO and ${\rm H_2}$ with varying ratios over a wide potential range.

Results and discussion

Powder X-ray diffraction (PXRD) was conducted to analyse the crystal structure of the Ti₃AlC₂, Ti₃C₂T_x and Au/Ti₃C₂T_x nanocomposites, as illustrated in Fig. 2. It depicts the PXRD patterns of Ti₃AlC₂ and Ti₃C₂T_x (before and after HF etching), respectively. It is evident that the Al present in the Ti₃AlC₂ max phase was successfully etched to yield Ti₃C₂T_x MXene (JCPDS no: 04-8738), as apparent from the disappearance of the Al peak at $2\theta \sim 39^\circ$. Furthermore, it is evident from Fig. 2 that the diffraction peak, which corresponds to the (002) plane at ~9.5°, shifted slightly towards lower angles, suggestive of the fading of Al intercalation.37 The XRD spectrum of Ti3C2Tx obtained after the HF-etching of the Ti3AlC2 sample correlated well with the literature. 38,39 PXRD reveals the crystalline nature of Au/Ti₃C₂T_x nanocomposites, composed primarily of Au and functional $Ti_3C_2T_x$ phases. The (111), (002), (022), and (113) crystal planes are linked to the broad and highly intense diffraction peaks at 38.3°, 44.5°, 64.7° and 77.8° that Au displays in the diffraction pattern. $Ti_3C_2T_x$ showed a shift in the positions of the peaks as a result of functionalization and composite effects. Previous studies have shown that $Ti_3C_2T_x$ possesses a substantial surface energy and very rich surface functional groups, such as -O, -OH and -F, which are advantageous to some substances to be adsorbed on its surface. 40,41 Finding all the key peaks of both Au and $Ti_3C_2T_x$ in the composite materials confirms the successful formation of the catalytically functionalised material.

To understand the valence bond states of $Au/Ti_3C_2T_x$ and $Ti_3C_2T_x$, XPS analysis was performed (Fig. 3 and Fig. S3†). The peaks between 454 and 457 eV indicate the potential presence

Paper Nanoscale

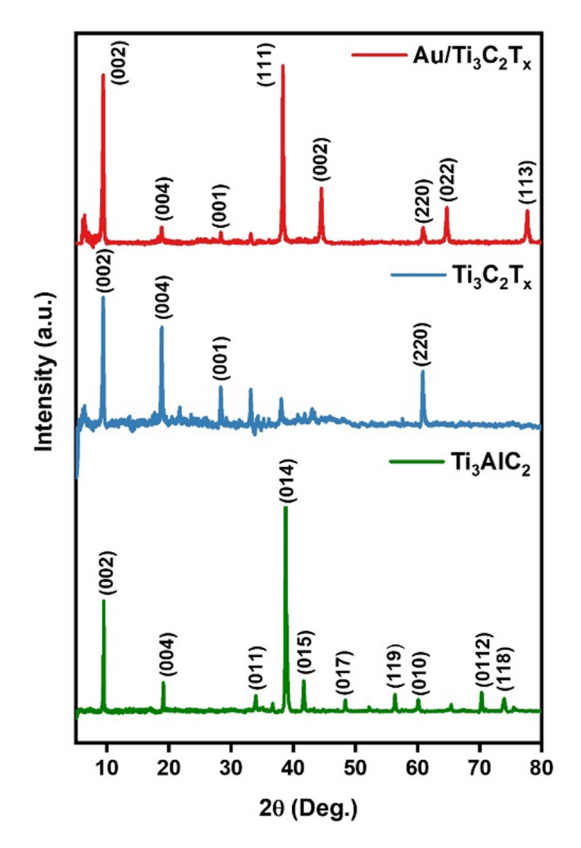


Fig. 2 The PXRD of Ti_3AlC_2 , $Ti_3C_2T_x$ and $Au/Ti_3C_2T_x$ composites.

of Ti low valence state species, including Ti(III) (~456.2 eV) (Fig. S3†). 42 Fig. 3a shows a complete survey spectrum of Au/ $Ti_3C_2T_x$ and illustrates the simultaneous existence of Au, C, Ti, O, and F elements. The high-resolution XPS spectra of Ti 2p, C 1s, Au 4f, O 1s, and F 1s are given in Fig. 3a-f respectively. 43 The two typical peaks of Ti 2p were observed at 459.4 eV and 465.1 eV, which are ascribed to Ti(IV) 2p_{3/2} and Ti(IV) 2p_{1/2}, respectively (Fig. 3b).44 This suggests that during the synthesis of Au/Ti₃C₂T_x, a transition from low valence levels of Ti(II and III) to the high valence level of Ti occurs, i.e., Ti(II and III) were converted to Ti(IV) (TiO2) (Fig. S3†). Fig. 3c displays the deconvoluted C 1s spectrum of Au/Ti₃C₂T_x. The peaks at 289.4 eV, 286.5 eV, 285.4 eV, and 281.8 eV are attributed to O-C=O, C-O, C-C, and C-Ti. 45 The deconvoluted Au 4f spectrum displays peaks at 83.9 and 87.6 eV, which are indicative of the reduced form of Au(0) with a distinct spin-orbit component ($\Delta = 3.7$ eV), Fig. 3d. 46,47 The result therefore suggests further that the Au NPs were successfully synthesized on the surfaces of Ti₃C₂T_x. As seen in Fig. 3e, the deconvoluted O 1s spectrum shows peaks at 530.6 eV and 532.1 eV, which can be matched with metal oxygen bonds (Ti-O and Ti-OH). 48 Moreover, oxygenated functional groups play a role in enhancing surface functionality and improving wettability and they provide a negatively charged surface. Similarly, Fig. 3f shows the deconvoluted F 1s spectrum, in which the peak at 685.0 eV was assigned to Ti-F. These results further indicate that AuNPs exist on the Ti₃C₂T_x substrate, which has oxide, hydroxide and fluoride functionalities on the surface.

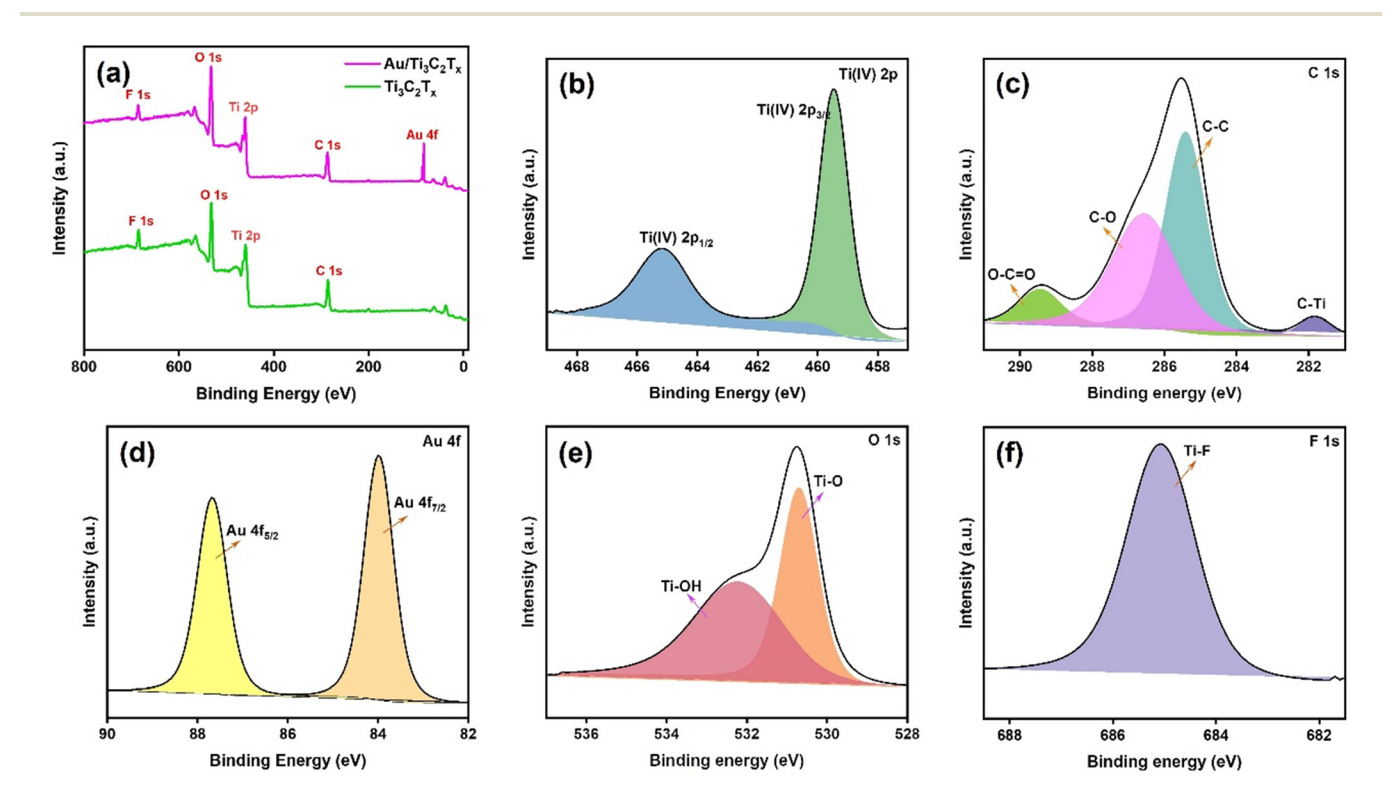


Fig. 3 (a) The full survey XPS spectrum, and (b) Ti 2p, (c) C 1s, (d) Au 4f, (e) O 1s and (f) F 1s spectra of $Au/Ti_3C_2T_x$.

Nanoscale Paper

The morphological features of $Ti_3C_2T_x$ MXene nanosheets are shown in Fig. 4. The SEM image of etched Ti₃C₂T_x-MXene (Fig. 4a) indicated that Ti₃C₂T_x was well delaminated and exhibited an "accordion-like" morphology. Furthermore, the SEM image showed that the as-prepared Ti₃C₂T_x was stacked with a few layers of nanosheets (Fig. 4b). The AuNPs were successfully integrated into the exfoliated MXene nanosheets, as shown by the SEM image in Fig. 4c. Furthermore, efficient

etching and integration are clearly seen in the EDX spectrum (Fig. S1†). Fig. 4d shows the remarkable transparency contrast of the 2D Ti₃C₂T_x thin sheets with the super carbon membrane, demonstrating their ultrathin nature. Fig. 4e shows the HR-TEM picture, which shows a lattice fringe spacing of 0.41 nm with the corresponding SAED pattern in the inset. The surface of 2D MXene thin sheets has uniformly dispersed AuNPs, as seen from the TEM image in Fig. 4f and the lattice

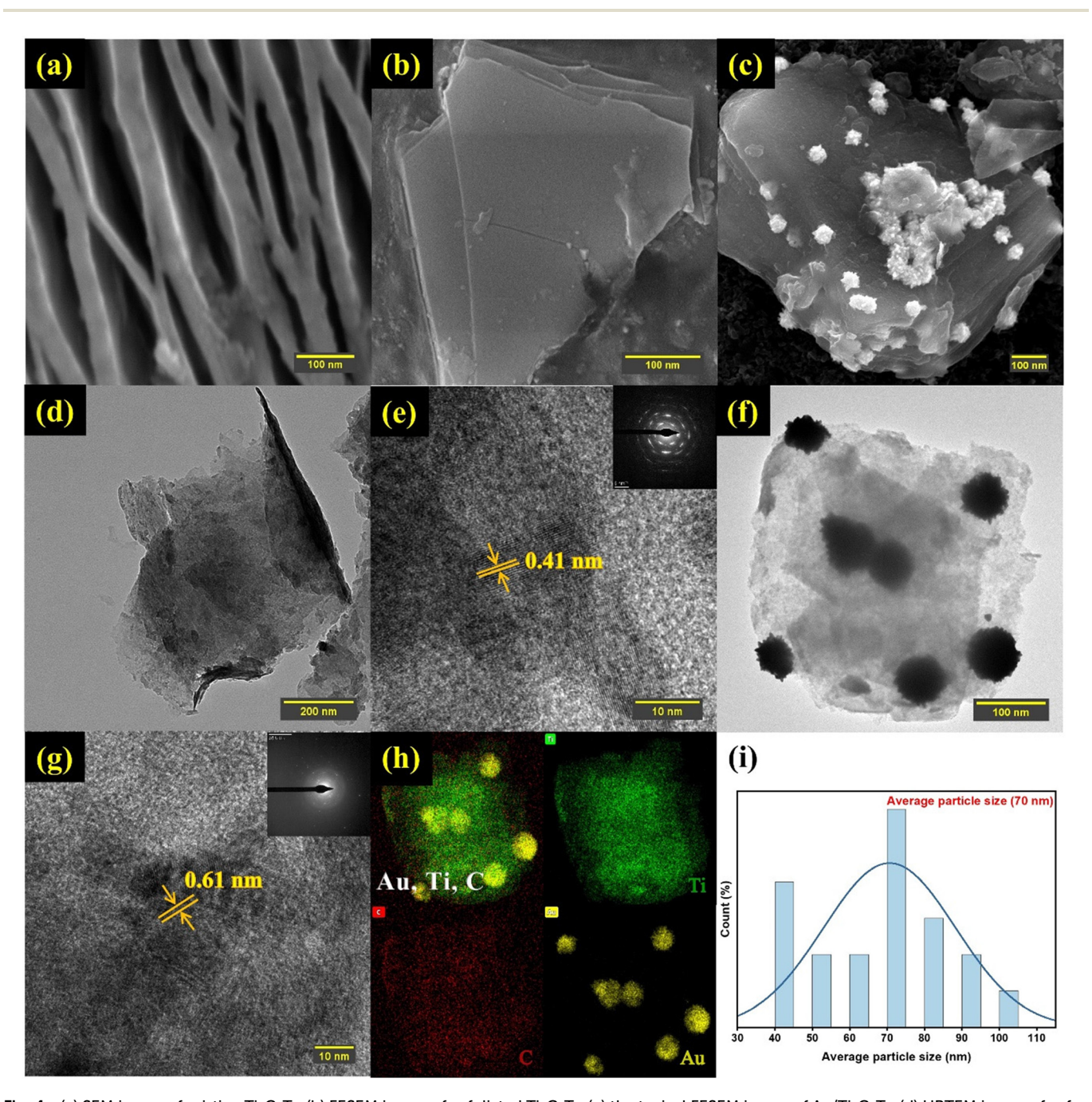


Fig. 4 (a) SEM image of pristine Ti₃C₂T_x, (b) FESEM image of exfoliated Ti₃C₂T_x, (c) the typical FESEM image of Au/Ti₃C₂T_x, (d) HRTEM image of exfo liated $Ti_3C_2T_x$, (e) TEM image of $Ti_3C_2T_x$, with the inset showing the SAED pattern, (f) HRTEM image of the $Ti_3C_2T_x$ /AuNPs composite, (g) TEM image of the $Ti_3C_2T_x/AuNP$ composite, with the inset showing the SAED pattern, (h) HAADF-TEM image of $Au/Ti_3C_2T_x$ and the corresponding EDS mapping, and (i) particle size distribution.

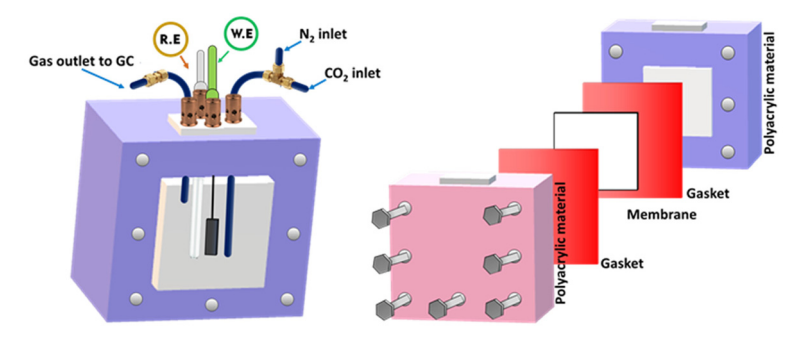


Fig. 5 Electrochemical cell used in the ECRR experiment.

fringe spacing is 0.61 nm, as seen from the HR-TEM picture in Fig. 4g. Additionally, the SAED pattern in the inset and the TEM image show that AuNPs were adhered to the MXene surface. EDS mapping analysis was performed to further validate the formation of the AuNPs and MXene assemblies (Fig. S2†). Fig. 4h shows the uniform distribution of AuNPs on the Ti₃C₂T_x thin sheets and the existence of Au, Ti, and C. According to the statistical TEM analysis of the Au/Ti₃C₂T_x composite (Fig. 4i), the average particle size was found to be 70 nm.

To assess the electrochemical performance of the MXene based catalysts in the co-conversion of CO2 and H2O to CO and H₂, electrochemical experiments such as cyclic and linear sweep voltammetry were conducted in 0.1 M KHCO₃ at ambient temperature and pressure. As shown in Fig. 5, an electrochemical cell was homemade and designed to collect the evolved gases from the working electrode compartment and inject them directly into the short-path of the gas chromatography valve for quantification. The catalyst's electrochemical behavior in the working solution was studied using Cyclic Voltammetry (CV) at 50 mV s⁻¹ with N₂. These voltammograms can be considered as blanks (Fig. S4a and S4b†). The corresponding electrocatalysts were tested over a range of potentials (0.6 to -1.4 V_{RHE}). Electrocatalytic activity under a N₂ flow can be attributed to either the hydrogen evolution reaction (HER) or catalyst reduction. Based on the voltammograms obtained with CO₂ saturation and under a positive pressure of CO₂, a reduction peak appeared at about -0.42 V vs. RHE (Fig. S4c†). This may be explained by the electron transfer mechanism caused by the adsorption intermediates formed during the CO₂ reduction. In terms of current densities measured at the same potentials, for the same catalyst, slightly higher activity is noted in the presence of CO₂ than in N₂. This enhanced outcome could be attributed to the electrochemical CO₂ reduction (Fig. 6a). The catalysts' electrocatalytic activity was greatly influenced by their composition in the following order: $Ti_3AlC_2 < Ti_3C_2T_x < Au/Ti_3C_2T_x$. In this regard, the Ti₃AlC₂ and Ti₃C₂T_x electrocatalysts exhibited cathodic current densities of 17.0 mA cm⁻² and 26.8 mA cm⁻², respectively, at -1.2 V vs. RHE, whereas the Au/Ti₃C₂T_x composite displayed a current density of 43.9 mA cm⁻² under identical conditions. When compared to the MAX phase Ti₃AlC₂ and pristine MXene $Ti_3C_2T_x$ electrocatalysts, the $Au/Ti_3C_2T_x$ composite showed significantly greater electrochemical activity.

Chronoamperometry (CA) was used to further investigate the electrochemical activity of these catalysts under ECRR conditions. The current-time transients are differentiated in Fig. 6b, where the CA was recorded for 60 minutes at E = -0.62V vs. RHE. The CA curves followed the same trend as the LSV curves, which confirms that the formed Au/Ti₃C₂T_x composite displays the highest activity among the prepared catalysts. Ensuring the durability of the electrocatalyst over extended periods is a crucial aspect and a primary requirement for commercialization. In this aspect, a thorough examination was conducted to assess the long-term stability of the Au/Ti₃C₂T_r composite over a span of 36 hours, at a constant potential of -0.62 V vs. RHE (Fig. S4d†). Following the 36 hours electroreduction period, no noticeable alteration in the current density was detected, indicating the exceptional stability of the Au/ Ti₃C₂T_x composite. The minor fluctuations observed in the chronoamperometry curve can be attributed to the formation and bursting of bubbles during continuous electrolysis, a phenomenon previously documented in similar investigations.

Furthermore, the ECSA of the $Au/Ti_3C_2T_x$ composite was determined by measuring its double layer capacitance (C_{dl}) using cyclic voltammetry at various scan rates (10 to 50 mV s⁻¹). The ECSA plot of the Au/ $Ti_3C_2T_x$ composite shows a maximum $C_{\rm dl}$ value of 153 μF cm⁻², as shown in Fig. S5,† suggesting that there are more electrocatalytically active sites than usual. This further supports the ECRR's exceptional performance. To further understand the improved electrochemical behaviors, electrochemical impedance spectroscopy (EIS) was carried out in a CO₂-saturated 0.1 M KHCO₃ solution on Au/Ti₃C₂T_x, Ti₃C₂T_x, and Ti₃AlC₂ over a frequency spectrum ranging from 100 mHz to 1 MHz, using an AC voltage amplitude of 10 mV at the open circuit potential as shown in Fig. 6c. $Au/Ti_3C_2T_x$ clearly exhibits a lower charge transfer resistance than Ti₃AlC₂ and Ti₃C₂T_x which is advantageous. This implies that Au/Ti₃C₂T_x has rapid charge transfer kinetics and the proposed electrical equivalent circuit could effectively fit all the EIS data (inset of Fig. 6c).

The performance and long-term stability of GDEs are also controlled by their wetting behaviour, which determines the presence and durability of gas-liquid-solid triple-phase Nanoscale Paper

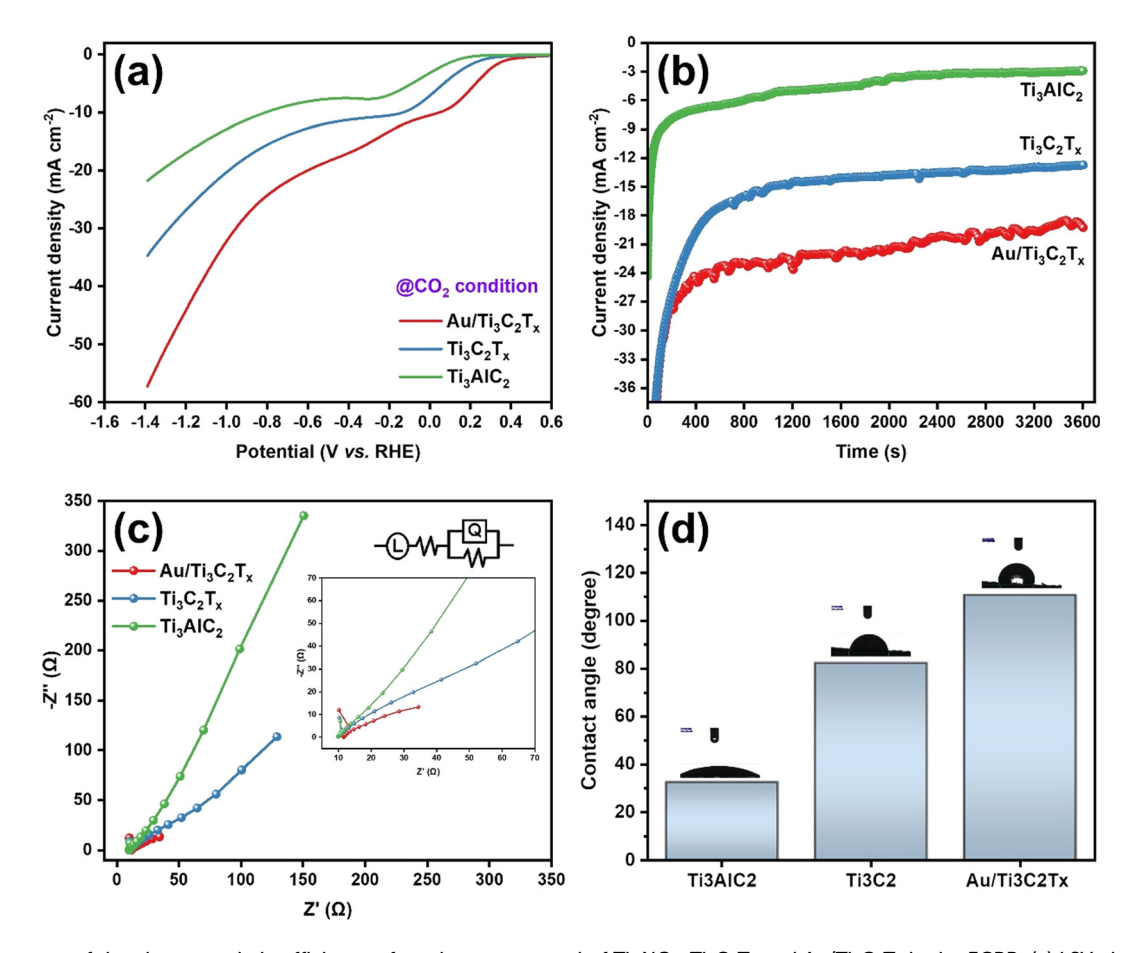


Fig. 6 Assessment of the electrocatalytic efficiency of catalysts composed of Ti₃AlC₂, Ti₃C₂T_x and Au/Ti₃C₂T_x in the ECRR: (a) LSV plots; (b) chronoamperometric responses at -0.62 V vs. RHE; (c) EIS conducted on Au/Ti₃C₂T_x, Ti₃C₂T_x, and Ti₃AlC₂. Inset: equivalent electrical circuit; and (d) contact angle.

barriers, in addition to their catalytic activity and accessible surface area. Two possible configurations for Au/Ti₃C₂T_x composite-coated GDEs in a zero-gap gas diffusion electrolyzer seem feasible: because the surface of the Au/ $Ti_3C_2T_x$ composites and their interior nanopores are fully wetted, there is a possibility that the electrolyte will enter the GDE; alternatively, the $Au/Ti_3C_2T_x$ composites will preferentially become wet due to their higher capillary forces. The composited Au/Ti₃C₂T_x surface may also exhibit hydrophobic properties when the surface structures of Au are at the micrometer scale. The hydrophobicity of Au/Ti₃C₂T_x composite-coated GDEs with nanoscale porosity achieved through compositing is significantly increased, as measured using contact angle measurements. Consequently, the hydrophobicity increased from \sim 32.6° for the Ti₃AlC₂ coating to \sim 110.7° for the Au/Ti₃C₂T_x composite coatings (Fig. 6d). Overall, the contact angle measurements exhibited high reproducibility across various regions of the Au/Ti₃C₂T_x composite-coated GDEs, indicating a high level of sample uniformity. It is noteworthy that the hydrophobic properties of Au/Ti₃C₂T_x composite coatings align with the finding that free-standing Au/Ti₃C₂T_x layers float on water. The hydrophobic GDE substrate may have a

bigger influence on the Au/Ti₃C₂T_x composite coating due to its higher contact angle than Ti₃C₂T_x.

The catalytic performance of Au/Ti₃C₂T_x composites and that of the resulting products were analyzed in detail during the ECRR on the Au/Ti₃C₂T_x electrode. The catalytic efficiency of the Au/Ti₃C₂T_x catalyst in the ECRR was assessed by contrasting the current densities obtained from LSVs in a 0.1 M KHCO3 electrolyte under N2-saturated and CO2-saturated conditions. The cathodic current observed in the N2-saturated solution was assigned to the Hydrogen Evolution Reaction (HER), whereas the cathodic current recorded in the CO₂-saturated solution encompassed contributions from both the HER and the ECRR (Fig. 7a). Consequently, the electrocatalytic activity for the ECRR decreased as the cathodic potential shifted from -0.22 V to -0.82 V vs. RHE.

The influence of the applied electrode potential on the electrochemical performance of the Au/Ti₃C₂T_x catalyst was further explored using chronoamperometry. Fig. 7b displays the CA curves recorded at -0.22, -0.32, -0.42, -0.52, -0.62, -0.72, and -0.82 V vs. RHE for 60 min. The disturbance observed in the recorded CA curve was due to the gas formation on the catalyst surface and the subsequent detachment Paper Nanoscale

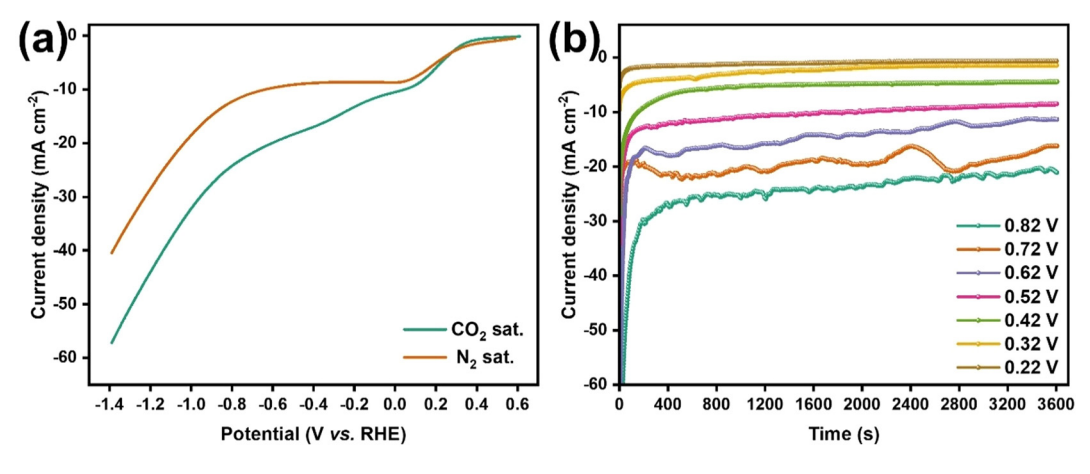


Fig. 7 Electrocatalytic activity of the $Au/Ti_3C_2T_x$ composites for the ECRR. (a) LSVs under CO_2 saturated and N_2 saturated conditions and (b) chronoamperometric curves at a potential of -0.22 V (brown) and -0.82 V (green) vs. RHE (colour on line).

of the formed gas bubbles from the electrode surface. Once the gas bubbles reach a sufficient size, they separate from the catalyst surface, resulting in a subsequent increase in current density. The applied cathodic potential increased from -0.22 to -0.82 V νs . RHE, increasing the steady-state current density, which was consistent with the LSV curves shown in Fig. 7a. Furthermore, the CA tests demonstrated that the Au/Ti₃C₂T_x composite exhibited great stability during the electrochemical reduction of CO₂.

Gaseous products generated in the course of the ECRR at the Au/Ti₃C₂T_x composites were analyzed using gas chromatography (GC), as shown in Fig. S6.† It was observed that CO and H₂ were the major products, and that only <1% of CH₄ was detected, as shown in Fig. S7.† Fig. 8 shows that the faradaic efficiency of the production of H₂ and CO is strongly dependent on the applied electrode potential. It varied from $-0.22~\rm V$

to -0.82 V vs. RHE. At a cathodic potential of -0.42 V vs. RHE, analysis revealed that syngas was the predominant product obtained with a higher faradaic efficiency of 48.3% for CO and 25.6% for H_2 . Different ratios of syngas were generated and this variation in the ratio might be useful for the production of numerous industrial compounds. NMR was utilized for the analysis of the aqueous products, uncovering that formate was obtained as a major product in the aqueous phase, as shown in Fig. S8.† The findings from both GC and NMR analyses support the conclusion that the ECRR using the $Au/Ti_3C_2T_x$ electrode primarily promotes the formation of syngas, a mixture of CO and H_2 , with a small amount of liquid products. The results further indicate that the ratio of syngas/liquid products may be adjusted by altering the applied cathodic potential.

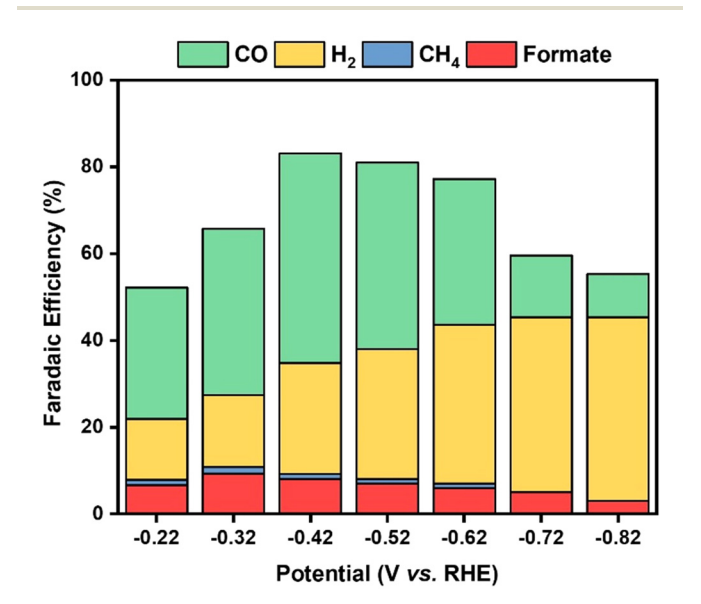


Fig. 8 Faradaic efficiency of ECRR products

Conclusions

A new Au/Ti₃C₂T_x electrocatalyst was prepared for application in the ECRR through an etching/fabrication process. The elemental compositions revealed by XRD and EDS analyses of the Au/Ti₃C₂T_x composites closely matched their surface compositions as determined by XPS, indicating uniformity of composition across the catalyst materials. The morphologies demonstrate that Au/Ti₃C₂T_x composites were significantly formed. The Au/Ti₃C₂T_x composite exhibited the highest electrocatalytic activity for the ECRR compared to Ti₃AlC₂ and Ti₃C₂T_x examined in this study. Also, an Au/Ti₃C₂T_x based gasdiffusion electrode was prepared and used as a cathode for the conversion of CO2 to CO owing to its improved electrocatalytic activity. GC analysis revealed that syngas was the predominant product obtained with a higher faradaic efficiency of 48.3% for CO and 25.6% for H_2 at a cathodic potential of -0.42 V vs. RHE. NMR analysis also revealed that formate was generated with a significant faradaic efficiency. Moreover, the EIS investigation demonstrated that Au/Ti₃C₂T_x composites exhibited significantly lower charge transfer resistance compared to the

other materials. In summary, the $\text{Au}/\text{Ti}_3\text{C}_2\text{T}_x$ composite presents itself as a compelling material with promising potential for applications in the production of synthesis gas from CO_2 . Further studies using this $\text{Au}/\text{Ti}_3\text{C}_2\text{T}_x$ catalyst towards the large-scale production of syngas and further optimization are underway.

Data availability

The data supporting this article have been included as part of the ESI.†

Conflicts of interest

The authors declare no conflict of interest.

Acknowledgements

The authors would like to thank the Director of CSIR-CECRI, Karaikudi, and staff members for their constant support and encouragement. Central Instrumentation Facility Division, CSIR-CECRI is acknowledged for characterization facilities. Dr M. K. acknowledges CSIR-FIRST (MLP-1004) for financial support. CECRI manuscript number: CECRI/PESVC/Pubs/2024-043.

References

- D. R. Feldman, W. D. Collins, P. J. Gero, M. S. Torn,
 E. J. Mlawer and T. R. Shippert, *Nature*, 2015, 519, 339–343.
- 2 S. Pacala and R. Socolow, Science, 2004, 305, 968-972.
- 3 S. Verma and A. Yadav, Energy Fuels, 2023, 37, 5712-5742.
- 4 G. Wang, J. Chen, Y. Ding, P. Cai, L. Yi, Y. Li, C. Tu, Y. Hou, Z. Wen and L. Dai, *Chem. Soc. Rev.*, 2021, 50, 4993–5061.
- 5 Z. Chen, X. Wang and L. Liu, *Chem. Rec.*, 2019, **19**, 1272–1282.
- 6 A. Prajapati, R. Sartape, M. T. Galante, J. Xie, S. L. Leung, I. Bessa, M. H. S. Andrade, R. T. Somich, M. V. Rebouças, G. T. Hutras, N. Diniz and M. R. Singh, *Energy Environ. Sci.*, 2022, 15, 5105–5117.
- 7 Y. Zhang, L.-Z. Dong, S. Li, X. Huang, J.-N. Chang, J.-H. Wang, J. Zhou, S.-L. Li and Y.-Q. Lan, *Nat. Commun.*, 2021, 12, 6390.
- 8 Q. Lu, K. Eid and W. Li, Nanomaterials, 2022, 12, 2379.
- 9 T. N. Nguyen and C.-T. Dinh, Chem. Soc. Rev., 2020, 49, 7488-7504.
- 10 F. P. García de Arquer, C.-T. Dinh, A. Ozden, J. Wicks, C. McCallum, A. R. Kirmani, D.-H. Nam, C. Gabardo, A. Seifitokaldani, X. Wang, Y. C. Li, F. Li, J. Edwards, L. J. Richter, S. J. Thorpe, D. Sinton and E. H. Sargent, *Science*, 2020, 367, 661–666.
- 11 B. Ambrose, R. Naresh, S. Deshmukh, M. Kathiresan and P. Ragupathy, *Energy Fuels*, 2023, 37, 18226–18242.

- H. Mistry, R. Reske, Z. Zeng, Z.-J. Zhao, J. Greeley,
 P. Strasser and B. R. Cuenya, J. Am. Chem. Soc., 2014, 136, 16473–16476.
- 13 W. Zhu, R. Michalsky, Ö. Metin, H. Lv, S. Guo, C. J. Wright, X. Sun, A. A. Peterson and S. Sun, *J. Am. Chem. Soc.*, 2013, 135, 16833–16836.
- 14 D. Gao, Y. Zhang, Z. Zhou, F. Cai, X. Zhao, W. Huang, Y. Li, J. Zhu, P. Liu, F. Yang, G. Wang and X. Bao, *J. Am. Chem. Soc.*, 2017, 139, 5652–5655.
- 15 W. Zhu, R. Michalsky, Ö. Metin, H. Lv, S. Guo, C. J. Wright, X. Sun, A. A. Peterson and S. Sun, *J. Am. Chem. Soc.*, 2013, 135, 16833–16836.
- 16 S. Back, M. S. Yeom and Y. Jung, ACS Catal., 2015, 5, 5089–5096.
- 17 W. Zhu, Y.-J. Zhang, H. Zhang, H. Lv, Q. Li, R. Michalsky, A. A. Peterson and S. Sun, *J. Am. Chem. Soc.*, 2014, 136, 16132–16135.
- 18 G. O. Larrazábal, A. J. Martín and J. Pérez-Ramírez, J. Phys. Chem. Lett., 2017, 8, 3933–3944.
- 19 K. Sun, T. Cheng, L. Wu, Y. Hu, J. Zhou, A. Maclennan, Z. Jiang, Y. Gao, W. A. Goddard, III and Z. Wang, *J. Am. Chem. Soc.*, 2017, 139, 15608–15611.
- 20 Y. Chen, C. W. Li and M. W. Kanan, J. Am. Chem. Soc., 2012, 134, 19969–19972.
- 21 X. Yan, C. Duan, S. Yu, B. Dai, C. Sun and H. Chu, Renewable Sustainable Energy Rev., 2024, 190, 114086.
- 22 B. Salah, K. Eid, A. M. Abdelgwad, Y. Ibrahim, A. M. Abdullah, M. K. Hassan and K. I. Ozoemena, *Electroanalysis*, 2022, 34, 677–683.
- 23 Y. He, W.-J. Jiang, Y. Zhang, L.-B. Huang and J.-S. Hu, J. Mater. Chem. A, 2019, 7, 18428–18433.
- 24 L. Zhang, Z. Wang, N. Mehio, X. Jin and S. Dai, *ChemSusChem*, 2016, **9**, 428–432.
- 25 Q. Lu, J. Rosen, Y. Zhou, G. S. Hutchings, Y. C. Kimmel, J. G. Chen and F. Jiao, *Nat. Commun.*, 2014, 5, 3242.
- 26 M. Naguib, M. Kurtoglu, V. Presser, J. Lu, J. Niu, M. Heon, L. Hultman, Y. Gogotsi and M. W. Barsoum, *Adv. Mater.*, 2011, 23, 4248–4253.
- 27 K. Rasool, M. Helal, A. Ali, C. E. Ren, Y. Gogotsi and K. A. Mahmoud, *ACS Nano*, 2016, **10**, 3674–3684.
- 28 A. Vijayaprabhakaran and M. Kathiresan, *Mater. Adv.*, 2023, 4, 3593–3602.
- 29 Y. Ibrahim, M. Meslam, K. Eid, B. Salah, A. M. Abdullah, K. I. Ozoemena, A. Elzatahry, M. A. Sharaf and M. Sillanpää, Sep. Purif. Technol., 2022, 282, 120083.
- 30 Z. Sun, T. Ma, H. Tao, Q. Fan and B. Han, *Chem*, 2017, 3, 560–587.
- 31 X.-Q. Tan, W. Mo, X. Lin, J. Y. Loh, A. R. Mohamed and W.-J. Ong, *Nanoscale*, 2023, **15**, 6536–6562.
- 32 D. Qu, X. Peng, Y. Mi, H. Bao, S. Zhao, X. Liu and J. Luo, *Nanoscale*, 2020, **12**, 17191–17195.
- 33 Z. Chen, X. Wang, J. P. Mills, C. Du, J. Kim, J. Wen and Y. A. Wu, *Nanoscale*, 2021, **13**, 19712–19739.
- 34 S. Verma, X. Lu, S. Ma, R. I. Masel and P. J. A. Kenis, *Phys. Chem. Chem. Phys.*, 2016, **18**, 7075–7084.

Paper Nanoscale

- 35 L.-C. Weng, A. T. Bell and A. Z. Weber, Phys. Chem. Chem. Phys., 2018, 20, 16973-16984.
- 36 H. Rabiee, L. Ge, X. Zhang, S. Hu, M. Li and Z. Yuan, Energy Environ. Sci., 2021, 14, 1959-2008.
- 37 W. Feng, H. Luo, Y. Wang, S. Zeng, L. Deng, X. Zhou, H. Zhang and S. Peng, RSC Adv., 2018, 8, 2398-2403.
- 38 Z. Li, L. Wang, D. Sun, Y. Zhang, B. Liu, Q. Hu and A. Zhou, Mater. Sci. Eng., B, 2015, 191, 33-40.
- 39 H. Fang, Y. Pan, M. Yin and C. Pan, J. Mater. Sci.: Mater. Electron., 2019, 30, 14954-14966.
- 40 F. Zhang, W. Liu, S. Wang, C. Liu, H. Shi, L. Liang and K. Pi, Composites, Part B, 2021, 217, 108900.
- 41 K. Tan, S. Liu, Y. Liu, L. Hou and C. Yuan, Nanoscale Adv., 2022, 4, 5253-5256.

- 42 S. S. Sangu, N. M. Illias, C. C. Ong, S. C. B. Gopinath and M. S. M. Saheed, BioNanoScience, 2021, 11, 314-323.
- 43 Z. Wu, D.-W. Sun, H. Pu, Q. Wei and X. Lin, Food Chem., 2022, 372, 131293.
- 44 H. Medetalibeyoglu, G. Kotan, N. Atar and M. L. Yola, Talanta, 2020, 220, 121403.
- 45 B. Wang, Q. Shu, H. Chen, X. Xing, Q. Wu and L. Zhang, Metals, 2022, 12, 2022.
- 46 Z. Zheng, W. Wu, T. Yang, E. Wang, Z. Du, X. Hou, T. Liang and H. Wang, J. Adv. Ceram., 2021, 10, 1061-1071.
- 47 H. Zhang, Z. Wang, F. Wang, Y. Zhang, H. Wang and Y. Liu, Anal. Chem., 2020, 92, 5546-5553.
- 48 K. Eid, Q. Lu, S. Abdel-Azeim, A. Soliman, A. M. Abdullah, A. M. Abdelgwad, R. P. Forbes, K. I. Ozoemena, R. S. Varma and M. F. Shibl, J. Mater. Chem. A, 2022, 10, 1965-1975.